Catalysis Science & Technology

ROYAL SOCIETY OF CHEMISTRY

PAPER

View Article Online
View Journal | View Issue

Cite this: *Catal. Sci. Technol.*, 2026, **16**, 2321

Insights into the monolayer formation on WO_3/TiO_2 catalysts for glycerol dehydration to acrolein

Martina Battisti, [ab] Nico Hollik,[b] Ansgar Meise, [c] Marc Heggen, [c] Chalachew Mebrahtu [ab] and Regina Palkovits [*ab]

Received 5th December 2025,
Accepted 9th February 2026

DOI: 10.1039/d5cy01485a

rsc.li/catalysis

The dehydration of glycerol to acrolein has the potential to increase the sustainability of acrolein production and its value chain. WO_3/TiO_2 has demonstrated good catalytic performance for this reaction, but an appropriate correlation of the catalyst properties with its activity is still missing. Thus, the influence of tungsten loading on WO_3/TiO_2 has been examined in terms of surface coverage and its subsequent effect on the catalyst acidity and activity. Different superficial species (monotungstates, polytungstates and crystalline WO_3) are present at different WO_3 loading as demonstrated using XRD, Raman, XPS and STEM. Moreover, increasing WO_3 loading resulted in enhanced Brønsted acidity, which positively impacted acrolein productivity. However, the formation of crystalline WO_3 at higher WO_3 loading compromises this positive effect by reducing the effective acid sites for acrolein formation.

Introduction

Transition of the fossil-based chemical industry toward environmentally sustainable approaches requires, among others, a switch to renewable feedstocks and circularity.[1] Hence, biodiesel demand has been rising since the 1990s and is forecast to continue growing in the coming years.[2] Since glycerol is a by-product of biodiesel production, this positive trend is expected to increase the availability of bio-glycerol, offering opportunities for its use as a platform chemical.[3] In particular, the dehydration of bio-glycerol to acrolein combines the need to find greener feedstocks for acrolein production and its value chain with the need to implement by-product valorization towards a circular economy. The gas-phase dehydration of acrolein has been performed on various acid catalysts, in particular zeolites,[4,5] supported heteropolyacids,[6] metal phosphates,[7] and metal oxides.[8] To date, only one comprehensive study of glycerol dehydration on WO_3/TiO_2 in a fixed-bed reactor has been reported in the literature.[9] After testing different WO_3 amounts, the authors reported that 13.9 wt% was the optimal WO_3 loading for the highest acrolein selectivity. However, no relationship between the catalytic activity and its properties was provided to explain this trend.

The effect of high total acidity and concentration of Brønsted acid sites on the acrolein productivity is a well-understood phenomenon in the literature for various solid acids.[10–14] However, a supported WO_3-based catalyst is well known to form a superficial two-dimensional tungsten oxide layer on the oxide support, and its molecular structure depends on the surface coverage.[15–17] This, in turn, affects the acidity and catalytic performance of the supported WO_3 catalyst. At low WO_3 loadings, tetrahedrally coordinated monotungstate species are present on the support. As the loading increases, these species evolve into distorted square pyramidal (WO_5) or pseudo-octahedral (WO_6) polytungstates, eventually forming a monolayer (4–4.5 $W_{at.}$ nm^{-2}).[16–21] Once above the "monolayer" threshold, crystalline WO_3 starts to form.[16,17]

As mentioned above, surface coverage of supported WO_3 influences not only its molecular structure but also its acidity.[22] The formation of strong Brønsted sites was directly correlated with the development of polymeric WO_x species at surface densities above 1.1 $W_{at.}$ nm^{-2}. Above this loading, the Brønsted acidity increases progressively with increasing WO_3.[22–25] Once the monolayer was reached, a decrease in the number of acid sites was observed at higher loading due to the presence of crystalline WO_3 nanoparticles.[19]

Based on existing literature on supported WO_3 catalysts, it can be hypothesized that the observed activity trend by Ulgen and Hoelderich for glycerol dehydration to acrolein is related to the surface coverage of the WO_3/TiO_2 catalysts and their resulting acidity.[9] However, detailed experimental evidence is required to draw a structure–activity correlation and provide a conclusion. Similar conclusions were reported for WO_3 supported on ZrO_2 and on Al_2O_3.[14,26,27] The WO_3 loading was

[a] *Institute for a sustainable Hydrogen Economy, Forschungszentrum Jülich GmbH, 52428 Jülich, Germany. E-mail: r.palkovits@fz-juelich.de*
[b] *Chair of Heterogeneous Catalysis and Technical Chemistry, Institute for Technical and Macromolecular Chemistry, RWTH Aachen University, 52074 Aachen, Germany. E-mail: palkovits@itmc.rwth-aachen.de*
[c] *Ernst Ruska-Centre for Microscopy and Spectroscopy with Electrons, Forschungszentrum Jülich GmbH, 52428 Jülich, Germany*

found to impact the strength and type of acidity of WO_3/Al_2O_3. The highest acrolein selectivity achieved with the catalyst at intermediate WO_3 loading was correlated to the higher amount of weak acid sites and Brønsted acidity of the material.

Hence, in this study, WO_3/TiO_2 catalysts with increasing WO_3 loadings (0 to 30 wt%) were prepared to evaluate the influence of surface coverage and acidity on the gas-phase dehydration of glycerol to acrolein. The surface coverage and acidity of the catalysts were characterized using various techniques such as XRD, Raman, STEM-EDX, XPS, and pyridine FTIR. The influence of WO_3 loading on the presence of superficial species and their subsequent effect on the Brønsted acidity was investigated. Finally, we present a correlation between the catalyst properties and their glycerol dehydration activity, particularly in relation to the acrolein productivity and the formation of major by-products, acetaldehyde and hydroxyacetone.

Experimental

Synthesis of the WO_3/TiO_2 catalysts

The WO_3/TiO_2 catalysts were synthesized by a wet impregnation method using a TiO_2 support material provided by Saint-Gobain NorPro (ST61120). Before use, the TiO_2 ST61120 was crushed in a ball mill (50 Hz, 4 min), calcined at 400 °C for 4 h (10 °C min^{-1}) and sieved below 80 μm. A solution was prepared by dissolving an appropriate amount of tungstic acid in a 0.5 M aqueous oxalic acid solution (OA : TA = 20 : 1). The solution was stirred at 80 °C overnight. Then, the appropriate amount of TiO_2 support was added, and the solution was stirred at 80 °C for 4 h. The solvent was removed using a rotary evaporator, and the product was further dried at 110 °C overnight. The dried catalyst was calcined at 600 °C for 6 h at a heating rate of 10 °C min^{-1}. The bare TiO_2 catalyst was treated at the same calcination temperature starting from the commercial TiO_2 support.

Material characterization

The W loading in the prepared catalysts was determined by ICP-OES. Analyses were carried out at Kolbe micro labs.

The nitrogen adsorption and desorption isotherms were measured at −196 °C with a Quadrasorb SI device (3P Instruments). Before the analysis, the samples were degassed for 3 h at 150 °C in a FloVac degasser. The specific surface area (SSA) was determined by the Brunauer–Emmett–Teller method in the 0.05–0.2 p/p^0 range.

For the X-ray diffraction (XRD) measurements of the powder samples, a D2 PHASER benchtop X-ray analyzer (Bruker) equipped with a Cu-Kα source was used. The diffractograms were recorded with 2θ = 10–90° and a step resolution of 0.02°. Phase identification was performed using data from the ICSD release 2024.1.

Raman spectra of the support and catalysts were acquired using a Raman RXN2 spectrometer equipped with a 785 nm laser. Each spectrum was acquired as an average of 10 scans, with a 5 s acquisition time per scan.

The total acidity was measured by NH_3 temperature-programmed desorption using a Micromeritics AutoChem 2950 device equipped with a thermal conductivity detector (TCD). The samples were first degassed at 500 °C under a helium flow (10 °C min^{-1} ramp, 50 mL min^{-1} flow, 30 min). Afterward, ammonia adsorption was performed at 50 °C for 20 min (10% NH_3 in He, 50 mL min^{-1}). Weakly adsorbed ammonia was removed at 50 °C under a helium flow (20 min, 50 mL min^{-1}). Finally, the TPD profile was recorded by ramping the temperature (10 °C min^{-1}) to 600 °C under a helium flow (50 mL min^{-1}).

Pyridine-FTIR measurements were acquired with a VERTEX 70 FTIR spectrometer equipped with an MCT detector. The catalysts (20 mg) were supported on a KBr pellet (80 mg) and mounted in a home-built transmission cell equipped with KBr windows. The sample was pretreated under vacuum at 250 °C for 2 h (5 °C min^{-1} ramp) and then cooled to 80 °C. Afterwards, pyridine adsorption was performed under vacuum for 4 min and equilibrated for 30 min without active vacuum. Physisorbed pyridine was then removed by applying vacuum at 150 °C for 30 min (5 °C min^{-1} ramp). FTIR spectra of the chemisorbed pyridine were recorded at 80 °C with an optical resolution of 2 cm^{-1} using the spectrum for the degassed catalysts as a background. The Brønsted/Lewis acid site ratio was calculated from the integrated peak areas of the Brønsted acid at 1540 cm^{-1} and the Lewis acid at 1450 cm^{-1} using their respective molar extinction coefficients (1.67 cm μmol^{-1} for the Brønsted acid and 2.22 cm μmol^{-1} for the Lewis acid).[28] Baseline correction was performed using the asymmetric least-squares smoothing method described by Eilers and Boelens.[29]

The amount of Brønsted and Lewis acid sites was quantified by combining pyridine-FTIR measurements with the total acidity estimated *via* pyridine adsorption in the liquid phase. The measurement was adapted from the basicity investigation of Al–Mg hydrotalcite with acrylic acid previously reported by our group.[30] For each experiment, 15 mg of catalyst (particle size <80 μm) was stirred overnight in 3 mL of a 0.2 mg g^{-1} pyridine solution in cyclohexane. The solutions were then filtered using a syringe filter (CHROMAFIL® Xtra PTFE-20/25) and analyzed using a Shimadzu UV 2600i spectrometer at a wavelength of 252 nm.

XPS measurements were performed using an AXIS Supra+ spectrometer (Kratos Analytical Ltd.) equipped with a hemispherical analyser and a monochromatized Al-Kα source (E = 1486.6 eV) operated at 15 kV and 225 W. During the measurement, the base pressure was <5.0 10^{-9} Torr, and a simultaneous charge neutralization (low-energy, electron-only source) was applied to compensate for charging effects. An emission current of 15 mA for both survey and high-resolution (C 1s, O 1s, W 4d, Ti 2p) scans was applied. During the measurement of the survey scans from 1200 to 0 eV, a pass energy of 160 eV and a step size of 1 eV was used (1 sweep, dwell time = 100 ms). For the high-resolution scans, a pass energy of 20 eV and a step size of 0.1 eV were applied (W 4d: 30 sweeps, dwell time = 115 ms; Ti 2p: 30 sweeps,

dwell time = 187 ms). CasaXPS Version 2.3.26PR1.0 was used for the evaluation of the data.

All obtained spectra were calibrated using the adventitious sp^3 C 1s peak (284.8 eV) as reference. Shirley background was applied to both W and Ti envelopes, and Lorentzian–Gaussian curves were used for the fitting (GL(90) and GL(30), respectively). For the Ti 2p, the position of the 2p 1/2 peak was set at 2p 3/2 + 5.72 eV, while its area was constrained at 0.5 times the area of the 2p 3/2. For the W 4d, both the 4d 5/2 and 4d 3/2 peaks were constrained to have the same FWHM, while the area of the 4d 3/2 peak was set at 2/3 of the area of the 4d 5/2. To calculate the surface W/(W + Ti) ratio, the full W 4d and Ti 2p envelopes were used, with the respective relative sensitivity factors. The following equation was applied:

$$\frac{W}{W+Ti} = \frac{\frac{A_{W\,4d}}{RSF_W}}{\frac{A_{W\,4d}}{RSF_W} + \frac{A_{Ti\,2p}}{RSF_{Ti}}}$$

$A_{W\ 4d}$ = area of the W 4d envelope
$A_{Ti\ 2p}$ = area of the Ti 2p envelope
RSF_W = relative sensitivity factor W 4d (RSF_W = 4.42)
RSF_{Ti} = relative sensitivity factor Ti 2p (RSF_{Ti} = 2.00)

The STEM samples were prepared by suspending the catalyst powder in DI water and drop-casting it on a holey carbon Cu TEM grid. After evaporating the water, the remaining hydrocarbon contamination was removed with a UV-based sample cleaner (Hitachi HT ZONETEM II). Aberration corrected scanning transmission microscopy (AC-STEM) was performed on a Hitachi HF5000 instrument operating at 200 kV and equipped with a spherical-aberration (Cs) probe corrector. The EDX measurements were performed on an Oxford Instruments Aztec EDS System with 2 Ultim Max TLE detectors.

Activity measurements

The catalyst powder was first pelletized to obtain particles with a particle size range of 500–355 μm. The appropriate mass of pellets was diluted with silicon carbide (356 μm) to achieve a total volume of 2.8 mL, which was then loaded in a tubular reactor with an internal diameter of 10 mm. The reactor was then heated to 280 °C and flushed with nitrogen (50 mL min^{-1}) for 1 h before the start of the reaction. A 20 wt% glycerol solution in water (0.181 mL min^{-1}) and synthetic air (30.9 mL min^{-1}) were premixed in an evaporator at 280 °C before entering the reactor. The contact time was set to 0.36 s, and the hourly space velocity (HSV) was around 15 000 mL h^{-1} g_{cat}^{-1} at 280 °C and 1 bar, unless otherwise specified. The reaction products were condensed in a cooled funnel maintained at 0–5 °C. The reaction was carried out for 7 h, with liquid products collected every hour for analysis. The collected liquid products were diluted with acetonitrile and then analysed *via* off-line gas chromatography using an Agilent 8890 gas chromatograph equipped with a BD-WAX Ultra Inert 60 m column and a flame ionization detector.

Productivity was calculated based on the following equation, while calculation of conversion and selectivity are reported in the SI:

$$P_{Product} = \frac{\dot{n}_{Product}}{m_{Catalyst}} \times MM_{Product} \times 1000$$

$P_{Product}$ = productivity of the product considered (mg h^{-1} g_{Cat}^{-1})
$\dot{n}_{Product}$ = product molar flow leaving the reactor (mol min^{-1})
$MM_{Product}$ = molar mass of the product (g mol^{-1})
$m_{Catalyst}$ = mass of catalyst in the reactor (g)

Results and discussion

Catalytic activity evaluation

The WO_3/TiO_2 catalysts with different WO_3 loadings were tested in the gas-phase dehydration of glycerol under comparable reaction conditions reported by Ulgen and Hoelderich (T = 280 °C, contact time = 0.36 s, HSV = 15 000 mL h^{-1} g^{-1}, 20 wt% aqueous glycerol, 0.6 O_2/glycerol ratio).[9] Fig. 1a depicts the average productivity of acrolein between 3 and 7 h time on stream (TOS), while the corresponding values of conversion and selectivity are presented in Fig. S1 and Tables S1 and S2 in the SI. The carbon balance for the tested WO_3/TiO_2 catalysts was in a reasonable range; for example, the 15 wt% catalyst achieved 80% (details are provided in Table S1 in the SI). Pure TiO_2 exhibits the lowest acrolein productivity, below 100 mg h^{-1} g^{-1}, which increased four times when WO_3 is added. Increasing the WO_3 loading from 5 to 20 wt% led to an increased acrolein productivity, from 330 to 417 mg h^{-1} g^{-1}. Further increase in WO_3 loading to 30 wt% resulted in a decrease in productivity. As shown in Fig. 1b, a clear trend in the distribution of the by-products is obtained for the WO_3-containing catalysts. The productivity of acetaldehyde, acetic acid, and acrylic acid increases as the catalyst loading rises from 5 wt% to 15 wt% but then declines at higher WO_3 loadings. In contrast, hydroxyacetone formation exhibits the opposite trend; higher for the catalysts with 5 wt% and 30 wt% WO_3, while it is not detected at 15 wt% WO_3 loading. Although the catalyst with 15 wt% WO_3 shows lower acrolein productivity compared to the 20 wt% (412 mg h^{-1} g^{-1} *vs.* 417 mg h^{-1} g^{-1}), its higher productivity for acetaldehyde, acetic acid, and acrylic acid suggests its highest overall activity. Furthermore, both the catalysts with 15 wt% and 20 wt% WO_3 loadings were tested at a higher HSV (120 000 mL h^{-1} g^{-1}), aiming at about 50% glycerol conversion (Fig. 1c, the corresponding conversion and selectivity values are reported in Fig. S2 and Table S3 (SI)). Accordingly, the 15 wt% WO_3/TiO_2 catalyst demonstrates a higher intrinsic acrolein productivity of 1320 mg h^{-1} g^{-1} compared to the 1180 mg h^{-1} g^{-1} over the 20 wt% WO_3/TiO_2 catalyst. Compared to the results obtained at lower HSV, lower hydroxyacetone productivity is obtained with the 15 wt% WO_3/TiO_2 catalyst. Under these conditions, acrylic acid was not detected while comparable acetaldehyde and acetic acid productivity was observed, both reaching 25 mg h^{-1} g^{-1} for 15 and 20 wt%

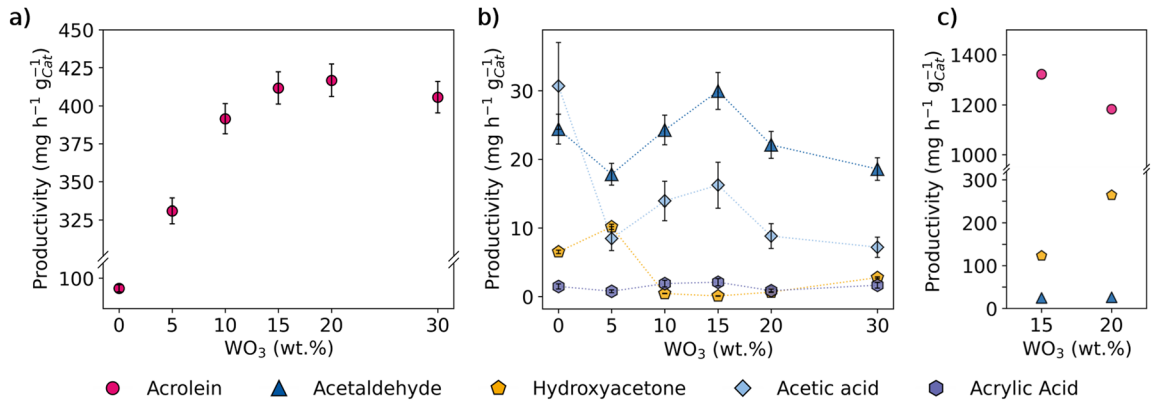

Fig. 1 Productivity of acrolein (a) and different by-products (b) for WO_3/TiO_2 catalysts with increasing WO_3 loading. Reaction conditions: T = 280 °C, contact time = 0.36 s, HSV 15 000 mL h^{-1} g^{-1}, 4.1 vol% glycerol, 83.6 vol% H_2O, 2.5 vol% O_2, 9.8 vol% N_2. (c) Productivity of acrolein and major by-products at a glycerol conversion of around 50%. T = 280 °C, contact time = 0.36 s, HSV 120 000 mL h^{-1} g^{-1}, 4.1 vol% glycerol, 83.6 vol% H_2O, 2.5 vol% O_2, 9.8 vol% N_2.

catalysts (acetic acid not shown in Fig. 1c to highlight the trends for the other products).

The catalytic activity results described here follow the trend already reported by Ulgen and Hoelderich, where acrolein selectivity rapidly increased with WO_3 loadings up to 14 wt% and then decreased with higher WO_3.[9] As mentioned above, this activity trend could be related to the catalysts' tungsten surface density reaching an optimum of around 14–15 wt% WO_3, which maximizes the number of active sites. Furthermore, the optimal acid properties of the catalyst at this WO_3 loading could contribute to the enhanced activity, as the dehydration of glycerol is strongly influenced by the acidity of the catalyst. Hence, to elucidate a structure–activity relationship, the tungsten surface density and acidity of the prepared catalysts were investigated and are discussed in detail in the next paragraphs.

Physicochemical properties

The WO_3 loading of the synthesised catalyst was determined using inductively coupled plasma analysis (ICP-OES) and is presented in Table 1. These measured WO_3 loadings align well with the nominal values used during the synthesis. Additionally, the calculated W surface density of the catalysts is given in Table 1 and will be discussed in detail in the following section. The values were calculated based on the measured WO_3 loading and the specific surface area of the TiO_2 support (detailed calculations provided in section 3 of the SI). N_2 physisorption was used to investigate textural properties of both TiO_2 and the catalysts, and the obtained specific surface areas (SSAs) are reported in Table 1. The SSA of the TiO_2 bare support was 105 m^2 g^{-1}, which decreased to 56 m^2 g^{-1} after calcination at 600 °C. For the WO_3/TiO_2 samples, SSA values ranged from 70 m^2 g^{-1} to 82 m^2 g^{-1}, with slightly higher values observed for the catalysts with 10, 15, and 20 wt% WO_3 loading.

Monolayer formation

Based on the literature, monolayer coverage of the support typically corresponds to a W surface density in the range between 4 and 4.5 $W_{at.}$ nm^{-2}.[19,20,31,32] Accordingly, the catalyst with 15 wt% WO_3 loading synthesized herein can be considered as a material with a "monolayer" coverage. It can therefore be expected that crystalline WO_3 forms on the catalyst at WO_3 loadings above 15 wt%, where the monolayer coverage is exceeded.[33] However, to confirm this trend on the monolayer formation, the prepared catalysts with different WO_3 loadings were characterized *via* XRD, Raman spectroscopy, XPS, and STEM.

Firstly, the evolution of crystalline WO_3 at increasing loadings was investigated using powder X-ray diffraction. As shown in Fig. 2a the major reflexes of anatase TiO_2 are obtained at 25°, 38° and 48° (ICSD-9852) for all the prepared catalysts.[34] No distinct reflexes of crystalline WO_3 are obtained up to 15

Table 1 WO_3 loading, calculated W surface density and specific surface area (SSA) for the synthesized catalysts after calcination at 600 °C

Catalyst	WO_3[a] (wt%)	Calculated W surface density[b] ($W_{at.}$ nm^{-2})	SSA[c] (m^2 g^{-1})
TiO_2	—	—	56.4
5 wt% WO_3/TiO_2	4.89	1.27	75.7
10 wt% WO_3/TiO_2	9.91	2.72	81.4
15 wt% WO_3/TiO_2	14.7	4.27	82.0
20 wt% WO_3/TiO_2	19.7	6.07	79.1
30 wt% WO_3/TiO_2	29.6	10.4	70.1

[a] WO_3 loading measured with ICP-OES. [b] Calculated W surface density based on the measured WO_3 loading and the SSA of the TiO_2 support. The calculation is reported in section 3 of the SI. [c] Specific surface area measured with N_2 physisorption.

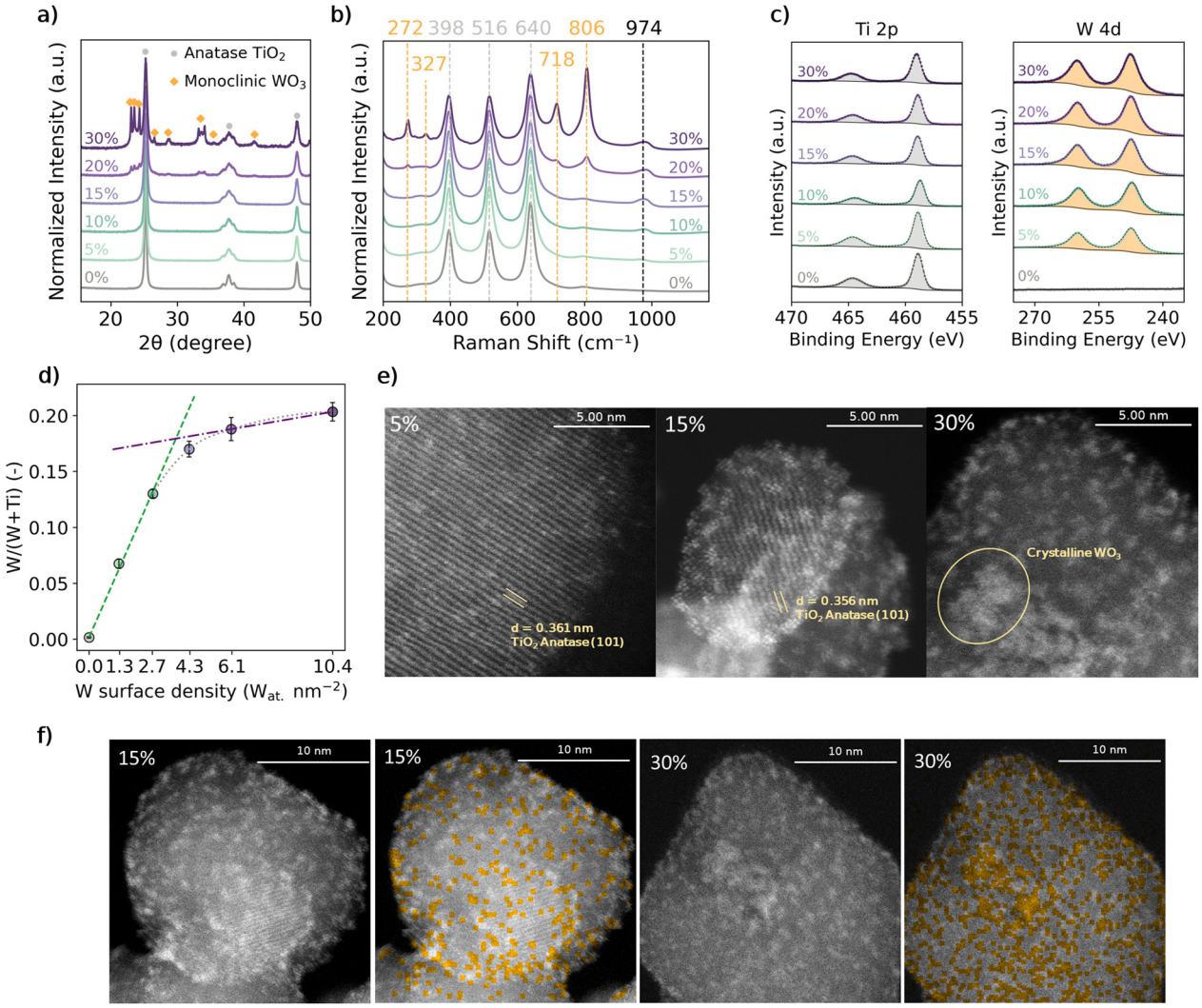

Fig. 2 (a) XRD patterns and (b) Raman spectra of WO_3/TiO_2 catalysts at increasing WO_3 loading; (c) XPS Ti 2p and W 4d high-resolution scans of the WO_3/TiO_2 catalysts. The envelope areas used for the evaluation are highlighted in the image. (d) Dependency of the surface W/(W + Ti) ratio (XPS) from the calculated W surface density (Table 1) for the WO_3/TiO_2 catalysts; (e) STEM dark-field images of the WO_3/TiO_2 catalysts with 5 wt%, 15 wt% and 30 wt% WO_3 loading; (f) STEM-EDX mapping of W Mα edge of 15 wt% and 30 wt% WO_3/TiO_2.

wt% loading, except the broadening of the anatase TiO_2 reflexes. For the catalysts with 20 wt% and 30 wt% WO_3 loadings, crystalline WO_3 reflexes are observed (ICSD-15905), indicating a loading exceeding the monolayer coverage.[35] Similar conclusions can also be drawn from the Raman spectra (Fig. 2b). For the anatase TiO_2, three strong peaks are present at 398, 516, and 640 cm^{-1}. A new peak develops at around 970–980 cm^{-1}, which is associated with the incorporation of WO_3 into the support. According to the literature, this is assigned to the symmetric stretching mode of terminal W═O bonds in bidimensional superficial tungsten oxide species, and it is indicative of the interaction between the tungsten oxide and the support.[17,33,36,37] At WO_3 loadings above 15 wt%, four new peaks appeared (*i.e.*, at 272, 327, 718, and 806 cm^{-1}), indicating again the presence of crystalline WO_3.

Moreover, XPS analysis is commonly reported as further proof of the monolayer coverage of supported WO_3 catalysts.[20,37–41] Hence, XPS measurements of all the WO_3/TiO_2 catalysts were performed, and the obtained spectra are presented in Fig. 2c. Due to the overlap between Ti 3p and W 4f, the Ti 2p and W 4d peak areas were used to calculate the surface W ratio as W/(W + Ti), as reported in the Experimental section. It is generally agreed that the surface W ratio measured *via* XPS increases linearly with the WO_3 loading and the calculated W surface density up to the monolayer limit, which is characteristic of a uniformly dispersed W phase.[37] Some studies indicated a deviation from this linearity at WO_3 loadings above the monolayer coverage,[37,41] while others still report a linear dependency with a lower slope[20,38,40] due to the decrease in W dispersion. For the catalysts prepared in this study, the trend of the surface W/(W + Ti) ratio based on the calculated W surface density (Table 1) is illustrated in Fig. 2d. At calculated W surface densities below 2.7 $W_{at.}$ nm^{-2}, a linear dependency is observed, indicating the high dispersion of the superficial W species (green dashed line in Fig. 2d). After 2.7 $W_{at.}$

nm^{-2} (10 wt% WO_3/TiO_2), the dependency starts to curve, indicating a decrease in the measured surface W/(W + Ti) ratio compared to the calculated W density (grey dotted curve in Fig. 2d). This decrease can be ascribed to the lower contribution of crystalline WO_3 to the W 4d peak compared to the dispersed WO_3, likely due to the differences in the electron escape depth between these two species. Based on the linear relationship at high loadings demonstrated by Yu *et al.* in their study on WO_3 dispersion over TiO_2,[20] a linear dependency is also interpolated for the catalysts with high WO_3 loading (violet dash-dotted line in Fig. 2d). The intersection of the two linear interpolations indicates the monolayer limit of the WO_3/TiO_2 catalyst, above which the WO_3 dispersion starts to decrease. The proximity of the intersection with the 15 wt% WO_3/TiO_2 catalyst (calculated W surface density of 4.3 $W_{at.}$ nm^{-2}) agrees with the assumption of this catalyst to have a monolayer coverage.

To visualize the superficial growth of WO_3 on the TiO_2 support at increasing WO_3 loadings, STEM images were collected below the monolayer (5 wt% WO_3/TiO_2), at the monolayer (15 wt% WO_3/TiO_2), and above the monolayer (30 wt% WO_3/TiO_2). The obtained dark-field images for all three catalysts are depicted in Fig. 2e. At low WO_3 loading (5 wt%), the WO_3 is not clearly distinguishable; only small bright spots are observed on the TiO_2. This is consistent with the presence of monotungstate species in tetrahedral coordination at low W surface coverage, which can lead to an almost atomically dispersed W species.[21] Once the monolayer coverage is reached (15 wt%), the development of polytungstate species results in the formation of small patches of WO_x. The bright agglomerates visible in the dark field are roughly below 1 nm in diameter, which is below the detection limit of XRD and corroborates the absence of crystalline WO_3 reflexes in the XRD pattern.[42] From the STEM images, the formation of an actual monolayer on the TiO_2 surface is unlikely to be observed. In contrast, the formation of small patches of polytungstate species homogeneously dispersed over the support surface was evident. When the WO_3 loading exceeds the monolayer coverage (30%), together with small WO_3 patches, larger and brighter areas are present. These larger WO_3 domains are likely responsible for the presence of crystalline WO_3, as already observed by XRD and Raman measurements of the 30 wt% WO_3/TiO_2. Furthermore, the WO_3 dispersion was further analysed using EDX mapping (W Mα), which is shown in Fig. 2f. The brighter areas that were identified using dark-field STEM for the 15% and 30% are confirmed to be associated with the presence of W. In particular, the big bright patch of the catalyst with 30% WO_3 loading corresponds to the presence of WO_3, as indicated by the stronger W Mα signal.

In summary, both XRD and Raman analysis reveal the presence of crystalline WO_3 at WO_3 loadings of 20 wt% or higher (≥6.5 $W_{at.}$ nm^{-2}), indicating that the monolayer threshold has already been exceeded. From the XPS measurements, the monolayer threshold appeared to be reached at 15 wt% WO_3 loading, while lower loadings showed higher WO_3 dispersion as confirmed by the STEM analysis. A low WO_3 loading results in the formation of isolated tungstate species, as highlighted by the absence of WO_3 domains. The WO_3 monolayer does not present as a continuous coverage of the support, rather as a well-dispersed multitude of polytungstate patches below 1 nm in diameter. Further increase of the WO_3 loading does not alter the monolayer dispersion but leads to the formation of bigger WO_3 crystalline domains.

Acidity investigation

Glycerol dehydration to acrolein is influenced by the amount, strength, and type of acid sites of the catalysts used. The total acidity of the catalysts was estimated using NH_3 temperature-programmed desorption. The obtained TPD profiles are reported in Fig. S4 (SI), while the corresponding desorbed ammonia quantification is reported in Fig. S5 (SI). All the catalyst samples show similar desorption profiles, with acidity values between 2.0 and 2.6 mmol g^{-1}. The type of acid sites was further investigated using pyridine-FTIR (Fig. 3a). According to the literature, the bands at 1450 cm^{-1} and 1540 cm^{-1} are commonly assigned to the Lewis acid sites (LAS) and Brønsted acid sites (BAS), respectively.[28] The pure TiO_2 support exhibits only Lewis acidity, while the incorporation of WO_3 into the support leads to the development of Brønsted acidity, as already reported for supported WO_3 systems.[24,43,44] Due to experimental limitations of the pyridine-FTIR, quantification of the BAS and LAS sites was not possible and only the Brønsted/Lewis sites

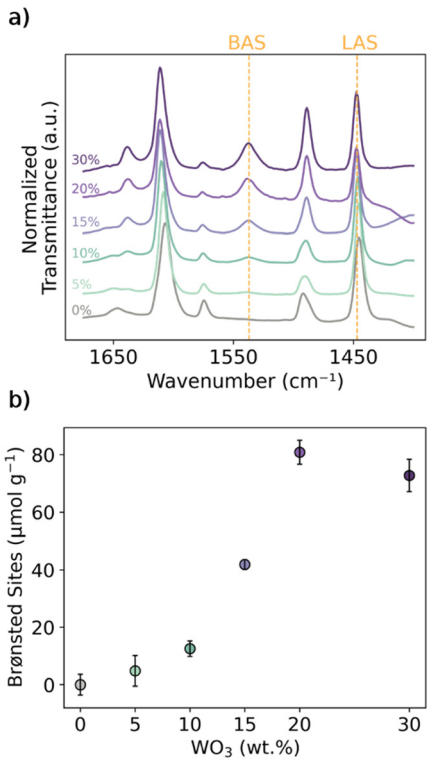

Fig. 3 (a) Pyridine-FTIR spectra of the WO_3/TiO_2 catalysts. Highlighted are the bands indicating Brønsted acidity (BAS) and Lewis acidity (LAS) that are used in the quantification. (b) Estimated Brønsted sites as a function of the WO_3 loading of the catalysts.

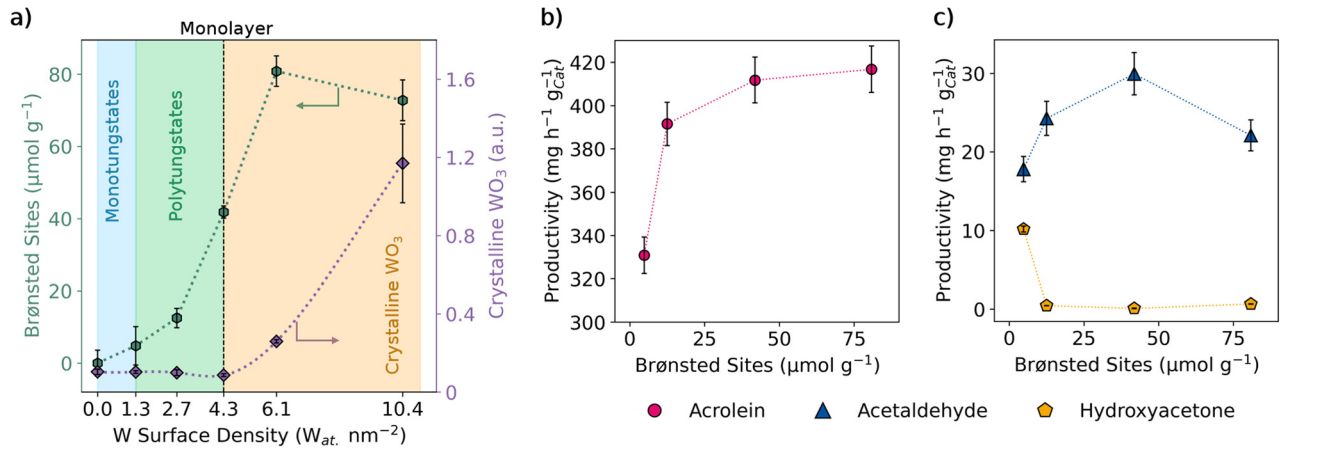

Fig. 4 (a) Brønsted sites and crystalline WO_3 – ratio of Raman peak's areas of WO_3 (~800 cm^{-1}) and TiO_2 anatase (515 cm^{-1}) – at increasing calculated tungsten surface density; the different areas of tungsten species are highlighted. (b) Acrolein and (c) acetaldehyde and hydroxyacetone productivity as a function of the Brønsted acidity of the WO_3/TiO_2 catalysts.

ratio was obtained. To estimate the BAS, the Brønsted/Lewis sites ratio was combined with the total amount of acid sites quantified with pyridine adsorption experiments (Fig. S6 (SI)). The findings are presented in Fig. 3b. A significant increase in the Brønsted acidity is observed with increasing WO_3 loadings up to 20 wt%, which presents the highest amount of BAS (81 μmol g^{-1}). Increasing the WO_3 loading to 30 wt% does not lead to a further increase in the Brønsted acidity of the material, which remains similar. These observations are in accordance with what has been reported in the literature for comparable supported WO_3 catalysts.[14,26,45]

Based on the literature, a change in the coordination of the WO_x superficial species with increasing WO_3 loading has been related to an increase in BAS.[25] Kitano *et al.* further demonstrated the formation of Brønsted acidity for supported WO_3 both at the WO_3–support interface and at the interface between the different WO_3 domains.[40] Thus, the maximum amount of BAS was obtained at the monolayer coverage, and similar conclusions were reported by Saito *et al.* and Chen *et al.*[23,44] Therefore, to clarify the trend in BAS formation and correlate with the WO_x species, a semi-quantitative Raman analysis was performed and correlated with the amount of BAS measured. Fig. 4a depicts the crystalline WO_3 formation as W surface density increases, measured by semi-quantitative Raman analysis (Fig. 2b) using the ratio between the area of the 800 cm^{-1} peak (WO_3) and the 515 cm^{-1} peak (TiO_2 anatase). From the pure TiO_2 up to 4.3 $W_{at.}$ nm^{-2}, the ratio is constant at around 0.1 (see footnote†), and starts increasing at surface densities above 4.3 $W_{at.}$ nm^{-2} (the catalyst with monolayer coverage). Based on the existing literature[16,17,19,20] and the analytics presented in this study, three distinct areas can be assigned, as highlighted in Fig. 4a: (1) below 1.3 $W_{at.}$ nm^{-2} (5 wt% WO_3/TiO_2), where atomically dispersed monotungstate species are present; (2) between 1.3 and 4.3 $W_{at.}$ nm^{-2} (5 to 15 wt% WO_3/TiO_2), where polytungstate species aggregate up to the monolayer limit, forming disordered patches below 1 nm diameter that do not show crystalline properties; and (3) above 4.3 $W_{at.}$ nm^{-2} (15 wt% WO_3/TiO_2), where the monolayer limit exceeds and forms bigger WO_3 crystalline domains.

Compared to the studies mentioned above, the catalysts prepared in this study exhibit the highest amount of BAS at a W surface density of 6.1 $W_{at.}$ nm^{-2}, which is above the monolayer formation (Fig. 4a). A possible explanation for this trend could be the different catalyst preparation method employed. In particular, Kitano *et al.* demonstrated that different calcination temperatures impact the Brønsted acid sites, while Boz *et al.* highlighted the impact of different impregnation solvents on the amount and type of acid sites.[13,40]

Structure–activity relationship

Glycerol dehydration is an acid-catalysed reaction characterized by a complex reaction network. Many parallel and consecutive reactions can occur due to the high reactivity of the products formed. Alongside the main observed products, such as acrolein, hydroxyacetone and acetaldehyde, other products have been observed and might become relevant based on the catalyst and reaction conditions chosen (*i.e.*, allyl alcohol, propionaldehyde, acetone…).[10,46–48] For clarity, Scheme 1 presents the reaction network for glycerol dehydration limited to the products observed and discussed in this work.

The dehydration of glycerol has been reported to proceed through two different pathways.[47,48] The removal of the secondary OH group results in the formation of the unstable intermediate 3-hydroxypropanal, which can further dehydrate to acrolein or form acetaldehyde through a retro-aldol reaction.[10,47,48] Dehydration of the terminal OH group generally leads to the formation of hydroxyacetone, which is considered

† The ratio is not zero due to the presence at 796 cm^{-1} of the first overtone of the 398 cm^{-1} peak of anatase, which is constant from the pure TiO_2 up to 15 wt% WO_3. The peak of crystalline WO_3 for the 20 and 30 wt% catalysts (806 cm^{-1}) overlaps with this existing peak.

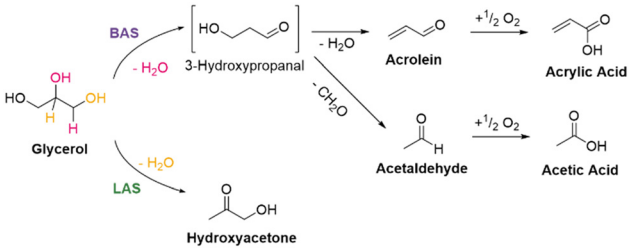

Scheme 1 Reaction network from glycerol to acrolein (main product), acetaldehyde and hydroxyacetone (main by-products), and to acrylic acid and acetic acid (oxidation of aldehydes).

stable under reaction conditions for glycerol dehydration.[12] The occurrence of these two reaction pathways depends on the type of acid in the catalyst.[49] The presence of Lewis acid sites has been linked to the formation of hydroxyacetone, as it favours the removal of primary OH groups. In contrast, Brønsted acid sites enhance the formation of acrolein (and acetaldehyde) by favouring the dehydration of secondary OH groups and the production of 3-hydroxypropanal.[12,49–51] The crucial role of the Brønsted acidity for acrolein production has been confirmed in recent investigations on WO_3/Al_2O_3.[14,27] The highest acrolein yield was achieved with the catalyst exhibiting the highest Brønsted acidity, resulting from the optimized WO_3 loading on the catalyst.[14]

Based on this hypothesis, a correlation between Brønsted acidity and acrolein productivity is presented in Fig. 4b. Moreover, the trend of main by-product formation (*i.e.*, acetaldehyde and hydroxyacetone) is also considered to confirm the reaction pathways mentioned in Scheme 1 (Fig. 4c). For a clearer comparison, only the region in which Brønsted acidity increases will be considered, corresponding to the catalysts with 1.3 to 6.1 $W_{at.}$ nm^{-2} (5 to 20 wt% WO_3/TiO_2). It is important to note that the reaction conditions selected for the activity tests are comparable to those reported in the literature.[9,13,52,53] Nevertheless, clear trends emerge because the catalyst properties affect product selectivity, and thus shifting productivity.

As shown in Fig. 4b, acrolein productivity strongly increases at low Brønsted acidity (below 25 μmol g^{-1}) as the monotungstate species transforms into polytungstate species. Conversely, further increases in the Brønsted acidity (above 25 μmol g^{-1}) result in a less pronounced increase in acrolein productivity. Additionally, the rise in Brønsted acidity with W surface coverage also results in higher acetaldehyde productivity, up to *circa* 50 μmol g^{-1} (Fig. 4c). This supports the hypothesis that acetaldehyde formation is favoured on BAS. However, BAS higher than 50 μmol g^{-1} result in a decline in acetaldehyde productivity. A possible explanation is that the BAS formed at the monolayer (up to 50 μmol g^{-1}) have a different nature than the BAS introduced with crystalline WO_3. The former are located at the interface between WO_3 and TiO_2 and form as a result of their interaction (interaction-BAS). We believe that these acid sites are responsible for the dehydration of glycerol to acrolein and acetaldehyde. The higher total Brønsted acidity of the 6.1 $W_{at.}$ nm^{-2} catalyst (20 wt% WO_3/TiO_2) is due to the introduction of new BAS present on the crystalline WO_3 (crystalline-BAS), which do not contribute to the reaction. The presence of high amounts of crystalline WO_3 results in the crystalline-BAS becoming dominant while also partially blocking the existing interaction-BAS. Hydroxyacetone productivity shows the opposite trend (Fig. 4c). Considerable productivity is only achieved at low BAS (5 μmol g^{-1}) while no hydroxyacetone formation was observed over the catalysts with higher Brønsted acidity. As mentioned above, hydroxyacetone formation competes with acrolein and acetaldehyde, and it is favoured over LAS (Scheme 1).[12] From the data presented herein, with increasing interaction-BAS density, the reaction pathway toward acrolein and acetaldehyde formation is favoured, and thus no hydroxyacetone is formed. Further increase in Brønsted acidity results in the formation of crystalline WO_3 and crystalline-BAS, which are not active in the reaction and likely hinder the accessibility of some of the active interaction-BAS, reducing acetaldehyde production. Consequently, the formation of hydroxyacetone becomes competitive again, and its productivity rises. A similar productivity trend is observed with the 30 wt% WO_3/TiO_2 catalyst. This high WO_3 loading does not significantly change the total amount of BAS compared to the 20 wt% WO_3/TiO_2 but forms more crystalline WO_3. Hence, the decrease in acetaldehyde and acrolein production results in a rise in hydroxyacetone productivity as its formation pathway is favoured again (Fig. 1a and b).

Based on these observations, we can conclude that the acrolein productivity is directly correlated with the increasing Brønsted acidity of WO_3/TiO_2 catalysts. However, excess BAS are linked with the formation of crystalline WO_3 and the introduction of not-active crystalline-BAS. The crystalline WO_3 influences the catalysts' selectivity, likely due to the partial blockage of the active interaction-BAS, favouring hydroxyacetone formation over acrolein and acetaldehyde.

Conclusions

This study investigated the effect of the tungsten loading in WO_3/TiO_2 catalysts on the formation of superficial species, the type of acidity, and catalytic activity in the glycerol dehydration reaction. At low WO_3 loading, well-dispersed isolated tungstate species are formed, as indicated by XPS and confirmed by STEM. The 15 wt% WO_3/TiO_2 catalyst best represented monolayer coverage, as evidenced by the correlation between the measured surface W/(W + Ti) ratio and the calculated W density. At WO_3 loadings of 20 wt% and higher, the formation of crystalline WO_3 was observed by both XRD and Raman measurements. The Brønsted acid sites formed by WO_3 incorporation into TiO_2 positively impact acrolein productivity. Among the prepared catalysts, the 20 wt% WO_3/TiO_2 catalyst possessed both the highest amount of Brønsted acid sites (80 μmol g^{-1}) and the highest acrolein productivity (417 mg h^{-1} g^{-1}). However, the presence of crystalline WO_3 on the catalyst with 20 wt% WO_3 favours the formation of hydroxyacetone, thereby hindering acrolein and acetaldehyde formation. In conclusion, the observed catalytic activity trend for glycerol dehydration over

the WO_3/TiO_2 catalysts with different WO_3 loadings resulted from the positive impact of increased Brønsted acidity at higher WO_3 loading, which is compromised by the effect of crystalline WO_3 formation.

Abbreviations

SSA Specific surface area
TOS Time on stream
HSV Hourly space velocity, calculated as the volumetric feed flow (mL h^{-1}) per mass of catalyst
BAS Brønsted acid sites
LAS Lewis acid sites

Author contributions

Martina Battisti: conceptualization, investigation, formal analysis, visualization, writing – original draft. Nico Hollik: investigation. Ansgar Meise: investigation. Marc Heggen: supervision. Chalachew Mebrahtu: conceptualisation, supervision, writing – review and editing. Regina Palkovits: supervision, writing – review and editing, funding acquisition.

Conflicts of interest

There are no conflicts to declare.

Data availability

Data for this article, including the raw data and the Jupyter Notebook documents used for data analysis, are available at Zenodo at https://doi.org/10.5281/zenodo.18618372.

Supplementary information (SI) is available. See DOI: https://doi.org/10.1039/d5cy01485a.

Acknowledgements

This work was funded by the German Federal Ministry of Research, Technology and Space (BMFTR) within Bio4MatPro-BL5-2: Green2Black (FKZ 031B1156). The support material was kindly provided by Saint Gobain NorPro. We acknowledge the support of Hitachi High-Technologies. Special thanks to Noah Avraham, Heike Bergstein, Carina Frantzen, Heike Fickers-Boltz, Hannelore Eschmann, Frederic Thilmany and Jens Heller for the technical help with the analytics; to Esther Dälken and Pia Groß for the help with TEM measurements; and to Matthias Urban and Nick Hausen for the help with XPS measurements.

Notes and references

1 United Nations Environment Programme, Green and Sustainable Chemistry: Framework Manual, 2020.
2 IEA, Biofuels - Energy System - IEA, https://www.iea.org/data-and-statistics/charts/global-biofuel-demand-in-transport-in-the-net-zero-scenario-2016-2030-2, (accessed 2 December 2024).
3 M. Pagliaro and M. Rossi, *The Future of Glycerol*, Royal Society of Chemistry, Cambridge, 2008.
4 T. Solos, N. Methiritthikul, C. Homla-or, P. Duangchan, K. Choojun and T. Sooknoi, *Catal. Sci. Technol.*, 2022, **12**, 5053–5066.
5 Y. T. Kim, K.-D. Jung and E. D. Park, *Appl. Catal., A*, 2011, **393**, 275–287.
6 E. Kraleva and H. Atia, *React. Kinet., Mech. Catal.*, 2019, **126**, 103–117.
7 G. Ruoppolo, G. Landi and A. Di Benedetto, *Catalysts*, 2020, **10**, 673.
8 V. Mahdavi and A. Monajemi, *RSC Adv.*, 2016, **6**, 114244–114255.
9 A. Ulgen and W. F. Hoelderich, *Appl. Catal., A*, 2011, **400**, 34–38.
10 S.-H. Chai, H.-P. Wang, Y. Liang and B.-Q. Xu, *Green Chem.*, 2007, **9**, 1130.
11 S. Suganuma, T. Hisazumi, K. Taruya, E. Tsuji and N. Katada, *ChemistrySelect*, 2017, **2**, 5524–5531.
12 A. Alhanash, E. F. Kozhevnikova and I. V. Kozhevnikov, *Appl. Catal., A*, 2010, **378**, 11–18.
13 I. Boz, M. S. Boroglu, Y. Zengin and B. Kaya, *Korean J. Chem. Eng.*, 2023, **40**, 1882–1891.
14 T. Aihara, K. Asazuma, H. Miura and T. Shishido, *RSC Adv.*, 2020, **10**, 37538–37544.
15 Y.-C. Xie and Y.-Q. Tang, *Adv. Catal.*, 1990, 1–43.
16 D. G. Barton, M. Shtein, R. D. Wilson, S. L. Soled and E. Iglesia, *J. Phys. Chem. B*, 1999, **103**, 630–640.
17 M. A. Vuurman, I. E. Wachs and A. M. Hirt, *J. Phys. Chem.*, 1991, **95**, 9928–9937.
18 F. Hilbrig, H. Schmelz and H. Knözinger, in *New Frontiers in Catalysis - Proceedings of the 10th International Congress on Catalysis, Budapest, 19-24 July 1992*, Elsevier, 1993, pp. 1351–1362.
19 T. Kim, A. Burrows, C. Kiely and I. Wachs, *J. Catal.*, 2007, **246**, 370–381.
20 X.-F. Yu, N.-Z. Wu, H.-Z. Huang, Y.-C. Xie and Y.-Q. Tang, *J. Mater. Chem.*, 2001, **11**, 3337–3342.
21 E. I. Ross-Medgaarden and I. E. Wachs, *J. Phys. Chem.*, 2007, **111**, 15089–15099.
22 T. Onfroy, V. Lebarbier, G. Clet and M. Houalla, *J. Mol. Catal. A: Chem.*, 2010, **318**, 1–7.
23 X. Chen, G. Clet, K. Thomas and M. Houalla, *J. Catal.*, 2010, **273**, 236–244.
24 T. Onfroy, G. Clet, S. Bukallah, T. Visser and M. Houalla, *Appl. Catal., A*, 2006, **298**, 80–87.
25 J. Bernholc, J. A. Horsley, L. L. Murrell, L. G. Sherman and S. Soled, *J. Phys. Chem.*, 1987, **91**, 1526–1530.
26 S.-H. Chai, B. Yan, L.-Z. Tao, Y. Liang and B.-Q. Xu, *Catal. Today*, 2014, **234**, 215–222.
27 R. Kanai, F. Yagi, K. Omata, H. Miura and T. Shishido, *Mol. Catal.*, 2023, **550**, 113588.
28 C. A. Emeis, *J. Catal.*, 1993, **141**, 347–354.
29 P. H. C. Eilers and H. F. M. Boelens, Baseline correction with asymmetric least squares smoothing, Leiden University Medical Centre Report, 2005, vol. 1, pp. 1–5.

30 I. Delidovich and R. Palkovits, *J. Catal.*, 2015, **327**, 1–9.
31 B. Zhao, X. Xu, J. Gao, Q. Fu and Y. Tang, *J. Raman Spectrosc.*, 1996, **27**, 549–554.
32 I. E. Wachs, *Catal. Today*, 1996, **27**, 437–455.
33 C. Martín, G. Solana, V. Rives, G. Marcì, L. Palmisano and A. Sclafani, *Catal. Lett.*, 1997, **49**, 235–243.
34 M. Horn, C. F. Schwerdtfeger and E. P. Meagher, *Z. Kristallogr.*, 1972, **136**, 273–281.
35 G. Andersson, B. Bak, A. Hillebert, H. Westermark, I. Steensgaard and T. Rosenberg, *Acta Chem. Scand.*, 1953, **7**, 154–158.
36 S. S. Chan, I. E. Wachs, L. L. Murrell, L. Wang and W. K. Hall, *J. Phys. Chem.*, 1984, **88**, 5831–5835.
37 R. B. Quincy, M. Houalla and D. M. Hercules, *Fresenius' J. Anal. Chem.*, 1993, **346**, 676–682.
38 T. Aihara, H. Miura and T. Shishido, *Catal. Sci. Technol.*, 2019, **9**, 5359–5367.
39 G. Lu, X. Li, Z. Qu, Q. Zhao, H. Li, Y. Shen and G. Chen, *Chem. Eng. J.*, 2010, **159**, 242–246.
40 T. Kitano, T. Hayashi, T. Uesaka, T. Shishido, K. Teramura and T. Tanaka, *ChemCatChem*, 2014, **6**, 2011–2020.
41 M. Kobayashi and K. Miyoshi, *Appl. Catal., B*, 2007, **72**, 253–261.
42 C. F. Holder and R. E. Schaak, *ACS Nano*, 2019, **13**, 7359–7365.
43 E. Hong, H.-I. Sim and C.-H. Shin, *Chem. Eng. J.*, 2016, **292**, 156–162.
44 M. Saito, T. Aihara, H. Miura and T. Shishido, *Catal. Today*, 2021, **375**, 64–69.
45 H. Song, X. Guo, Y. He, Y. Li, G. Liu, G. Yang and N. Tsubaki, *Catal. Today*, 2025, **460**, 115476.
46 W. Suprun, M. Lutecki, T. Haber and H. Papp, *J. Mol. Catal. A: Chem.*, 2009, **309**, 71–78.
47 E. Tsukuda, S. Sato, R. Takahashi and T. Sodesawa, *Catal. Commun.*, 2007, **8**, 1349–1353.
48 J. Deleplanque, J.-L. Dubois, J.-F. Devaux and W. Ueda, *Catal. Today*, 2010, **157**, 351–358.
49 F. Fernandes Barbosa and T. Pinheiro Braga, *ChemCatChem*, 2023, **15**, e202200950.
50 H. Park, Y. S. Yun, T. Y. Kim, K. R. Lee, J. Baek and J. Yi, *Appl. Catal., B*, 2015, **176–177**, 1–10.
51 J. Ding, C. Yan, T. Ma, R. Shao, W. Xu and P. Wang, *Can. J. Chem. Eng.*, 2019, **97**, 1152–1159.
52 R. Condotta, E. L. Gomes, D. A. de Freitas and J. G. R. Poco, *Ind. Eng. Chem. Res.*, 2025, **64**, 4300–4308.
53 J. Liu, X. Zhao, W. Wang, Y. Yan, G. Huang, M. Liang, X. Feng and W. Ji, *RSC Adv.*, 2025, **15**, 9801–9809.

